coatings

MDPI

Article

Three-Dimensional Point Cloud Stitching Method in Infrared Images of High-Voltage Cables

Guang Yu [1], Yan Huang [2,*] and Yujia Cheng [1,*]

[1] Mechanical and Electrical Engineering Institute, University of Electronic Science and Technology of China, Zhongshan Institute, Zhongshan 528400, China; yuguang@zsc.edu.cn
[2] School of Materials and Energy, University of Electronic Science and Technology of China, Chengdu 611731, China
* Correspondence: hyansworld@163.com (Y.H.); chengyujia@zsc.edu.cn (Y.C.); Tel.: +86-0760-8826-9835 (Y.C.)

Abstract: High-voltage power cables are crucial to the normal operation of all electrical equipment. The insulation surrounding these cables is subject to faults. The traditional methods for detecting cable insulation characteristics primarily focus on breakdown performance tests. However, the measurement precision is low, the risk coefficient is high, and the test cost is high. Additionally, it is difficult to precisely pinpoint high-voltage cable faults. Therefore, in this study, a method for inspecting high-voltage cable faults using infrared stereoscopic vision is proposed. This method enables non-contact remote safety measurements to be conducted. For a limited lens angle in an infrared camera, an area matching stitching method that incorporates feature point matching is developed. The key technologies for three-dimensional (3D) point cloud stitching include feature point extraction and image matching. To address the problem of the Harris algorithm not having scale invariance, Gaussian multi-scale transform parameters were added to the algorithm. During the matching process, a random sampling consistency algorithm is used to eliminate incorrect pairs of matching points. Subsequently, a 3D point cloud stitching experiment on infrared cable images was conducted. The feasibility of the stitching algorithm was verified through qualitative and quantitative analyses of the experimental results. Based on the mechanism by which thermal breakdowns occur, a method for detecting anomalous temperatures in cables is developed based on infrared stereoscopic vision. In this manuscript, the infrared technique, 3D point cloud stitching, and cables inspection are combined for the first time. The detection precision is high, which contributes to the development of high-voltage electrical equipment nondestructive testing.

Keywords: high-voltage cables; cable insulation; temperature anomalies; infrared images; feature point extraction; 3D point cloud stitching

Citation: Yu, G.; Huang, Y.; Cheng, Y. Three-Dimensional Point Cloud Stitching Method in Infrared Images of High-Voltage Cables. *Coatings* **2024**, *14*, 1079. https://doi.org/10.3390/coatings14091079

Academic Editor: Je Moon Yun

Received: 16 June 2024
Revised: 12 July 2024
Accepted: 29 July 2024
Published: 23 August 2024

1. Introduction

With the implementation of smart-grid projects, industrial electricity has been vigorously developed worldwide [1,2]. Currently, the three major characteristics of electricity transmission are its long range, high capacity, and low loss [3]. These are also used to evaluate the electric power industry level in a given country [4]. High-voltage transmission is a key component of power operations, and the insulation characteristics of high-voltage cables directly determine the operating efficiency of electric power systems [5]. During the operation of electric power equipment, cable insulation breakdowns can have serious consequences. To ensure the normal operation of power systems, cable insulation safety must first be guaranteed [6]. However, the cable installation position is high, which requires testing personnel to attend to them. In addition, modern insulation materials do not exhibit significant temperature changes. Thus, in daily maintenance, the testing personnel cannot easily detect them [7,8]. If the insulation breaks down under normal conditions, then the points at which this occurs are small and difficult to distinguish. The most frequently used

tools for measuring the temperatures of the cable surfaces are infrared thermometers [9]. However, their measurement precision is low and their security risk is higher. In contrast, using infrared stereoscopic vision to detect anomalous temperatures is a safe and effective method.

The operating principle of infrared stereoscopic vision is based on the fact that different surface temperatures produce infrared rays with different intensities [10]. According to the conversion of analog electronic signals in infrared cameras, different infrared images are shown, which contribute to follow-up testing. Infrared stereoscopic vision has many advantages, such as a high measurement efficiency, wide detection range, non-contact detection, and high safety factor. Therefore, infrared stereoscopic vision technology is widely used for the thermal detection of power equipment [11,12]. In the 1980s, the Luxtron Corporation in the USA developed a fluorescence fiber-optic colorimeter that could measure the surface temperature of high-voltage equipment, such as transformers, in real time. In addition, many electricity companies in Europe have developed a complete range of infrared detection standards for power equipment [13,14]. NDC Infrared Engineering in the USA has proposed that infrared thermal imagers can replace thermometers for power equipment detection [15,16]. Infrared thermal imagers offer the advantages of a wide detection range and low error rate, which improves the work efficiency [17]. High-voltage cables are commonly researched in infrared imaging technology because of the height of the transmission lines and their complex external environments. However, because of the angles involved, the working conditions of a long-distance cable cannot be displayed completely by a single image using traditional infrared detection technology [18,19]. The principle of 3D point cloud stitching is integrating the point cloud coordinates in all local coordinate systems to the same coordinate system. Hence, by combining infrared detection technology with image stitching technology, the working conditions of an entire high-voltage cable can be determined, enabling anomalous temperature detection to be more efficient.

Based on the above considerations, in this study, an infrared camera was used in place of a thermometer for measuring the temperature of high-voltage cables via infrared images [20,21]. Based on the infrared color depth, the cable surface temperature was obtained using the built-in function of the infrared camera. According to stereoscopic vision detection technology, the infrared cable images captured from multiple angles were combined to form a three-dimensional reconstruction [22,23]. Image stitching technology was used to restore the complete morphological characteristics of the tested cables [24]. Using the stitched images, the exact locations of the cable temperature anomalies were accurately located. If a cable malfunction occurs, the points at which the cable breaks down will be small and difficult to distinguish. Nevertheless, these points can be investigated using the previously detected anomalous temperatures [25,26]. In addition, the search range was decreased, which improved the detection efficiency of the cable breakdown points. These points can then be rectified using cable maintenance techniques, such as cold-shrinkage cable joint connections [27,28]. Furthermore, a series resonance power supply device (PSU) was built. For the infrared stereoscopic vision detection experiment, the cables were made of three typical insulation materials: pure low-density polyethylene (LDPE), nano-ZnO/LDPE, and nano-methylcyclopentadienyl manganese tricarbonyl (MMT)/LDPE. After electrification, the temperature anomalies in the high-voltage cables were accurately located, which demonstrates the method's enhanced efficiency in cable temperature anomaly detection and maintenance.

The rest of this paper is organized as follows. Section 2 describes the key technology used to stitch infrared cable images. Section 3 explains the infrared stereo vision technique used to detect cable breakdown points. Finally, Section 4 contains the conclusions.

2. Key Stitching Technology of Infrared Cable Images

When a cable's working condition is detected by an infrared camera, the restrictions inherent in the camera lens prevent the cable from being imaged at every angle in a single

shot [29]. Instead, each three-dimensional (3D) measurement is processed by point cloud stitching, from which the complete image of the tested cable is restored. In this study, a stitching method with high stitching accuracy, fast speed, and easy calculation is proposed based on cable measurement characteristics. This method significantly improved the stitching efficiency of the infrared cable images.

2.1. Infrared Camera Calibration Experiment

In this study, the calibration experiment conducted on the infrared camera was based on Zhang's calibration method, which incorporates corner subpixel-level extraction. Binocular stereo vision was selected as the camera measurement model. From Zhang's self-calibration, the calibration template is taken from multiple angles. In the case of a stationary camera, the angles of calibration template can be changed optionally. In the calibration experiment, the internal reference of the infrared camera is a fixed quantity. The external reference is a variation. These references can be calculated by Equation (1).

$$Z_c \begin{bmatrix} u \\ v \\ 1 \end{bmatrix} = \begin{bmatrix} \alpha_x & 0 & u_0 & 0 \\ 0 & \alpha_y & v_0 & 0 \\ 0 & 0 & 1 & 0 \end{bmatrix} \begin{bmatrix} R & t \\ 0^T & 1 \end{bmatrix} \begin{bmatrix} X_w \\ Y_w \\ Z_w \\ 1 \end{bmatrix} = M_1 M_2 X_w = M X_w \quad (1)$$

In Equation (1), M is the 3×4 order matrix combined by M_1 and M_2. M_1 is the internal reference matrix of the infrared camera. This matrix relates to the structural parameters of the infrared camera, including α_x, α_y, u_0, and v_0. M_2 is the external reference matrix of the infrared camera, which relates to the infrared camera external position in the measurement system. The external reference includes rotation matrix R and translation vector T. The essence of camera calibration is to calculate all internal and external references of the camera.

In this experiment, calibration board images were acquired using two infrared cameras, each of which captured 20 images. The calibration board had a hollow checkerboard pattern. During image acquisition, the calibration template was placed close to the heater tube. The temperatures in the hollowed-out and non-hollowed-out areas of the calibration board differed, and an obvious chromatic aberration was observed. When the infrared images were converted to grayscale images, the maximum values of the grayscale change were used as feature points. The infrared cameras were kept at consistent positions in the optical guideway. Subsequently, the location of the calibration board was changed. The experimental results were accurately calculated using the calibration toolbox in the MATLAB 2022 software package.

The process used to calibrate the infrared cameras was as follows.

(1) Data initialization. The memory space was partitioned (including the memory space for feature point coordinates and the calibration parameters of the infrared camera).
(2) Determination of corner point locations. Each infrared camera obtained 20 images at different angles. During the feature point extraction process, if the detection was successful, a nonzero result was returned, and the data for the feature points were stored. If the detection failed, zero was returned, and the program displayed an error and ended. Eighteen feature points were extracted from each calibration board.
(3) Feature point extraction. Feature points at the subpixel level were extracted.
(4) Coordinate storage. After the feature points at the subpixel level were extracted, the coordinate information was stored in the memory space.
(5) The image and spatial coordinate points were substituted into the linear constraint conditions. The intrinsic and extrinsic parameters of the infrared camera were calculated using the Zhang calibration method.
(6) Measurement error. The tested 3D space coordinates of one feature point were converted and the corresponding coordinates in the dimensional images were obtained. These data were then compared to the actual coordinates in the dimensional images.

The feature point extraction results obtained from the infrared camera calibration experiment are shown in Figure 1.

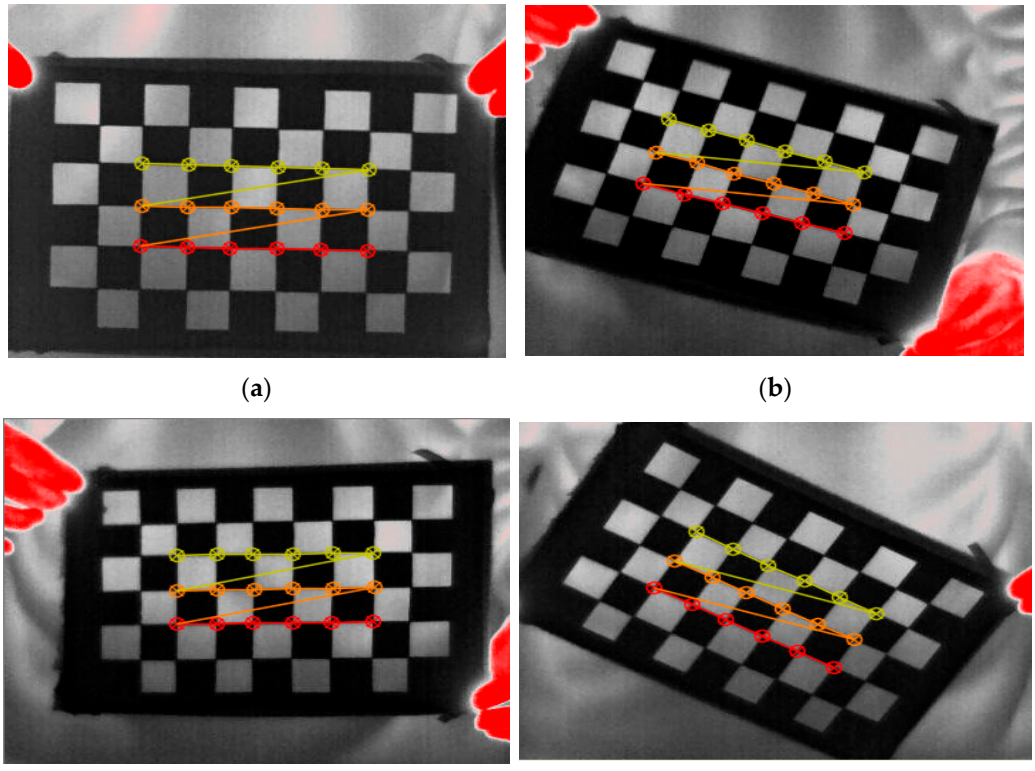

Figure 1. Renderings of the feature point extraction of the infrared calibration board: (**a**) position 1; (**b**) position 2; (**c**) position 3; (**d**) position 4.

The parameter calculation results for the two infrared cameras were as follows. First, the parameter calculation results for the infrared camera on the left side of the optical axis were

$$A_1 = \begin{bmatrix} 1668.58 & 0 & 191.20 \\ 0 & 1617.74 & 143.64 \\ 0 & 0 & 1 \end{bmatrix} \quad (2)$$

$$T_1 = \begin{bmatrix} -110.99 & -35.89 & 1231.62 \end{bmatrix} \quad (3)$$

The parameter calculation results for the infrared camera on the right side of the optical axis were

$$A_2 = \begin{bmatrix} 1494.22 & 0 & 191.64 \\ 0 & 1476.59 & 144.56 \\ 0 & 0 & 1 \end{bmatrix} \quad (4)$$

$$R_2 = \begin{bmatrix} -0.011231 & 0.987524 & -0.043275 \\ 0.999889 & 0.010521 & -0.022417 \\ -0.010137 & -0.113217 & -0.989421 \end{bmatrix} \quad (5)$$

$$T_2 = \begin{bmatrix} -245.69 & -58.36 & 1194.45 \end{bmatrix} \quad (6)$$

After calibration, the average error projection was used to evaluate the accuracy of the calibration results. The average error projections of the feature points are shown in Figure 2. The average calibration parameter errors of the two infrared cameras were 0.13617 and 0.13751 pixel, respectively. The measurement accuracy of this method was 17% and 11% higher than those of the direct linear method and Tsai's two-step method [30], respectively.

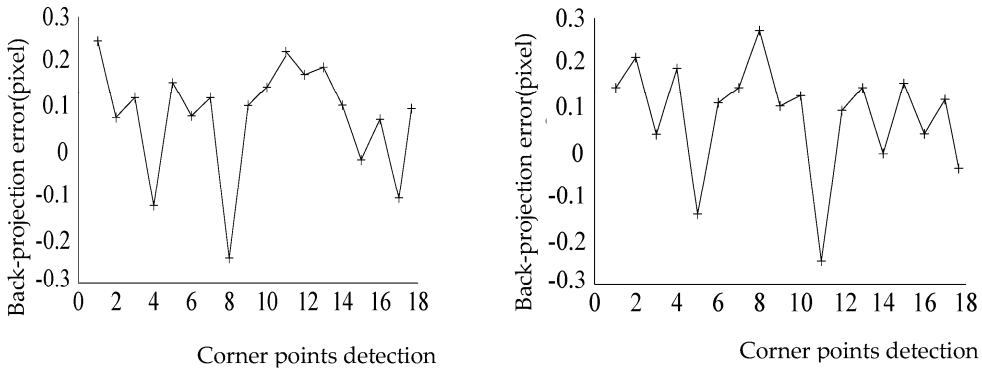

Figure 2. Re-projection error diagram of the image points: (**a**) reprojection error diagram of the left panel; (**b**) reprojection error diagram of the right panel.

2.2. Feature Point Detection Based on Multi-Scale Harris Operator

Corners, curvature maximum points, and line intersections are frequently used as feature points [31]. Because the tested cable surfaces were smooth and their appearances were homogeneous, the corners were selected for feature point extraction from the cable images. There are three common operators for extracting corners from 3D images: the Susan, Harris, and Moravec operators [32]. The corners extracted by the Susan operator had no obvious effect on the noise, and the detection accuracy was high. However, this algorithm is complex and its calculation time is long. The algorithm for extracting corners using the Moravec operator is simple and fast. However, it is easily affected by noise and its detection accuracy is low. The algorithm for extracting corners using the Harris operator is relatively simple and fast, and the extracted corners are uniformly distributed. Additionally, the corner quality is high, which can eliminate interference such as rotation and illumination. The corner extraction can also achieve accuracy at the subpixel level.

In this study, the corners of the infrared cable images were extracted using the Harris operator. If the gray value of one point varied widely from that of other nearby points, this point could be set as a corner [33]. The corners extracted by the Harris operator are expressed by

$$R = \det(C) - ktr^2(C) \tag{7}$$

where

$$C(x) = \begin{bmatrix} I_u^2(x) & I_{uv}(x) \\ I_{uv}(x) & I_v^2(x) \end{bmatrix} \tag{8}$$

$\det(C)$ and $tr^2(C)$ are the determinant and trace of the matrix $C(x)$, respectively; $I_u(x)$ and $I_v(x)$ are the image point partial derivatives in u and v directions, respectively; $I_{uv}(x)$ is a secondary mixed partial derivative; and k is an empirical constant in the range 0.04–0.06. Next, a threshold T is set. If $R > T$, this image point is extracted as a corner.

During the cable image stitching experiment, images of the tested cables were captured at different angles because the Harris operator does not exhibit scale invariance. However, the algorithm is sensitive to scaling and the rate at which the feature points are repeated is low, which is not suitable for image-matching experiments on infrared cables. To solve this problem, Gaussian multi-scale transform parameters were added to the Harris algorithm. The concrete steps used to extract the corners were as follows.

Gaussian multi-scale transform parameters were added to the infrared images. Next, a scale space was built. The extreme values in the local area were randomly selected. If the extreme value was higher than the set threshold, it was used as the original selection point.

The partial derivatives in the u- and v-directions of the original selection point were handled by a convolution operation with a Gaussian convolutional kernel (with a standard deviation of $s\sigma_n$), which is expressed by

$$\left\{ \begin{array}{l} I_u(x, s\sigma_n) = I(x) * G_u(x, s\sigma_n) \\ I_v(x, s\sigma_n) = I(x) * G_v(x, s\sigma_n) \end{array} \right\} \tag{9}$$

where s is a constant greater than one, and G_u and G_v are the Gaussian convolutional kernel of the partial derivatives in the u- and v-directions, respectively.

The matrix $C(x)$ in the Harris operator is given by

$$C(x, \sigma_1, \sigma_D) = \sigma_D^2 G(\sigma_1) * \left[\begin{array}{cc} I_u^2(x, \sigma_D) & I_{uv}(x, \sigma_D) \\ I_{uv}(x, \sigma_D) & I_v^2(x, \sigma_D) \end{array} \right] \tag{10}$$

where σ_1 and σ_D represent the scaling parameter and differential scale, respectively; $\sigma_1 = \sigma_D = s\sigma_n$; and $G(\sigma_1)$ is a Gaussian function.

Comparing the values of R and T, the corners under the scale of σ_n were calculated. Because all the cable surfaces were similar, the corners easily aggregated and dispersed unevenly. In this study, adjacent points were eliminated for corner extraction. A 3×3 pixel search area was used to extract the corners. If there was more than one corner within this area, the R values of these corners were compared. The corner with the maximum R value was the final corner selected. Examples of 3D stereoscopic infrared images of two adjacent cables are shown in Figure 3.

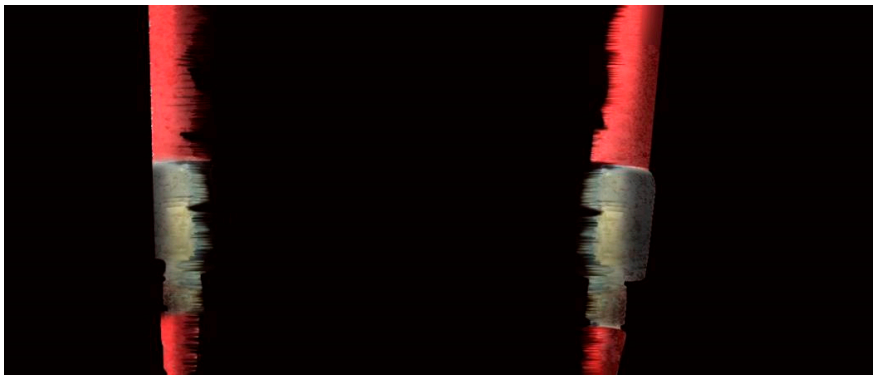

Figure 3. 3D stereoscopic infrared images of adjacent cables.

The experimental corner extraction results obtained using the multi-scale Harris operator are shown in Figure 4. According to the qualitative analysis, the corner extraction in the 3D stereoscopic infrared images of the cables was complete. Thus, the detection efficiency was excellent.

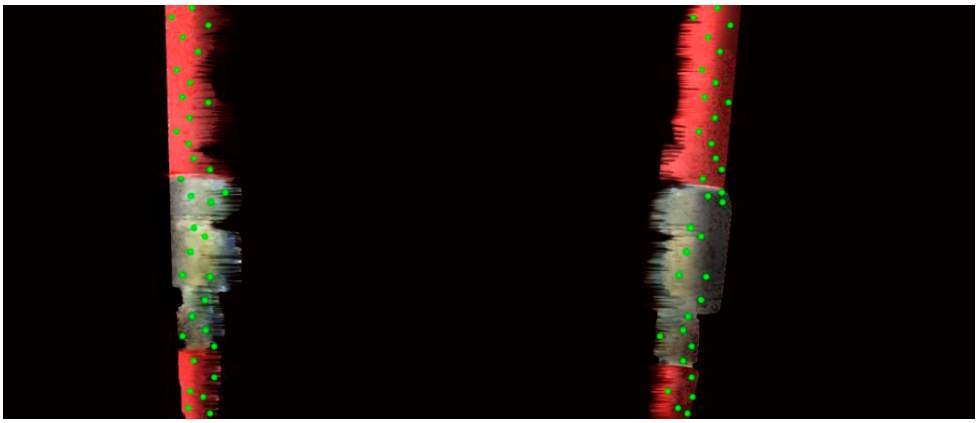

Figure 4. Corner points extracted using the multi-scale Harris operator.

2.3. Stitching Method Combining Area Matching and Feature Points Matching

Common image stitching methods can be categorized as one of two types. One is based on area matching and the other is based on feature point matching. For area matching, the common areas between two stitching images are used as the reference template from which similar regions in the two stitching images are identified. This method is easy to implement and its matching speed is high. However, it is affected by illumination and rotation. There are many similar regions in infrared cable images. The random selection template block causes a significant matching error, which affects the stitching precision. In feature point matching, the feature is extracted primarily from a common area. First, the two stitched images are subjected to feature matching. Subsequently, the transformation relationship between the two images is calculated. These features can be classified as points, edges, and surfaces. Image matching based on feature point gray value changes is the most common method, as it involves simple calculations, its operational speed is high, and it is insensitive to changes in illumination. In 3D infrared cable images, each point is similar, and a mismatch between the feature points can occur. In summary, the two commonly used stitching methods exhibit disadvantages during the stitching process and do not satisfy the requirements of high-accuracy infrared cable image stitching experiments.

Using the characteristics of 3D point cloud stitching of infrared cable images, this study proposes an improved algorithm that combines area matching with feature point matching. The stitching process of this algorithm is illustrated in Figure 5.

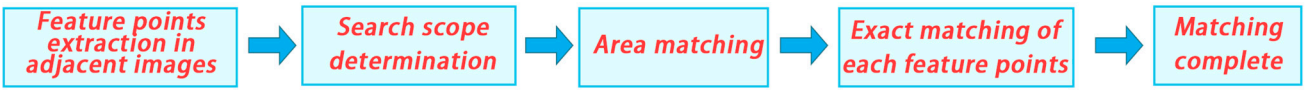

Figure 5. Proposed stitching method based on the combination of area matching and feature point matching.

The steps of this algorithm are summarized as follows. First, the feature points in the area common to two adjacent images are extracted. Subsequently, in one image, a template block with a suitable number of feature points is selected. In the other images, the common area is searched. Based on the principle of area matching, the matching block corresponding to the template block is determined and set as the initial matching value. According to the gray values of the image feature points, all feature points in the common area are matched accurately, after which the image stitching experiment is completed.

2.4. Area Matching of Feature Points

A model of the feature point area matching is shown in Figure 6. The common areas in the two stitched images are shown as shaded areas. In Figure 6a, the matching area is represented by the template block M. An adjacent image is shown in Figure 6b, in which the search area is represented as S. In the search area, a block of the same size as the template block M is shown, which is represented as S_j. By comparing the feature similarity between M and S_j, the accurate matching position in the search areas can be determined.

The concrete steps used in the feature point area matching process were as follows.

(1) In one tested image, the matching block range in the common area was set according to the feature point distribution characteristics in the stitching common area. The size of the matching block was determined based on the feature point arrangement density. An excessively large matching block affected the matching speed, and an excessively small matching block decreased the matching precision. Therefore, selecting an appropriately sized matching block was important. Under normal conditions, the number of matching blocks was set as an odd number. In general, there were 3–9 feature points in each matching block. Next, the feature point quantity N in the matching block, the value R in each feature point, and their exact locations were recorded accurately.

(2) The search range was limited to the common area of the matching images. During image acquisition, the movement of the two matching images was accurately recorded

using a binocular vision-measuring instrument. The search range was determined from this movement, which decreased the computation time to a certain extent.

(3) The corresponding matching block was searched in other tested images, and the test results were validated. The feature point quantity N in the matching block was compared to the feature point quantity N_i in the search area of the other tested images. Then, a threshold T was set. If $N_i - N \geq T$, the matching block area detected errors, and matching block detection must be performed. If $N_i - N \leq T$, the test results must be verified further. In the matching blocks of the two areas, the feature point quantity and R value of each feature point were compared. When the information was identical, the search range was successfully matched.

(**a**) (**b**)

Figure 6. Region matching model: (**a**) reference image; (**b**) search image.

After area matching, the matching speed of the 3D infrared cable image was boosted, which satisfied industrial measurement demands. The feature point area matching results for the 3D stereoscopic infrared cable images are shown in Figure 7. There are three feature points in the matching block.

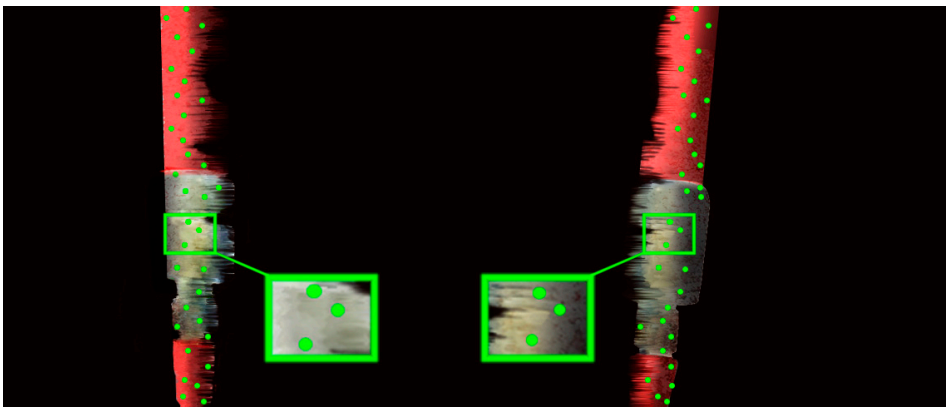

Figure 7. Region matching result of infrared cables image.

2.5. Exact Matching of Feature Points

After the area matching of the feature points, the matching positions of the two images were generally determined. For the exact matching of the feature points, all feature points in the matching block were matched individually, through which the exact location of the image stitching was located. The exact matching of the feature points was then realized.

In this study, the normalized cross-correlation (NCC) method was used for exact feature point matching. In this method, image matching was based on the gray value similarity between feature point neighborhood pixels. This method is insensitive to brightness changes and satisfies the demands of image stitching at different angles.

In the matching block, one of the feature points was randomly selected as the center point. In its neighborhood, a $(2N + 1) \times (2M + 1)$ detection window was defined, where

N and M are constants. Then, the feature points in the matching block were matched one by one. In one image, the feature point was p_1 and its neighborhood detection window was W_1. In the other image, the feature point was p_2 and its neighborhood detection window was W_2. The two window sizes were equal. The average gray values of the two windows were u_1 and u_2, and (x_1, y_1) and (x_2, y_2) were the image coordinates of the two feature points. The NCC is expressed as

$$NCC = \frac{\sum(W_1(x_1, y_1) - u_1)(W_2(x_1, y_1) - u_2)}{\sqrt{\sum(W_1(x_1, y_1) - u_1)^2 \sum(W_2(x_1, y_1) - u_2)^2}} \quad (11)$$

The single feature point with the maximum correlation coefficient was the matching point. Some incorrect pairs of matching points appeared in the matching process, which affected the stitching precision. An appropriate threshold 0.65 was set to eliminate incorrectly matched point pairs [34]. This threshold was used as the reference value for the maximum correlation coefficient. If the maximum correlation coefficient was less than the threshold, the matching point pairs were considered incorrect and were removed. Next, the feature point reverse matching method was used to further eliminate incorrect point pairs. The matching results for the two tested images are shown in Figure 8.

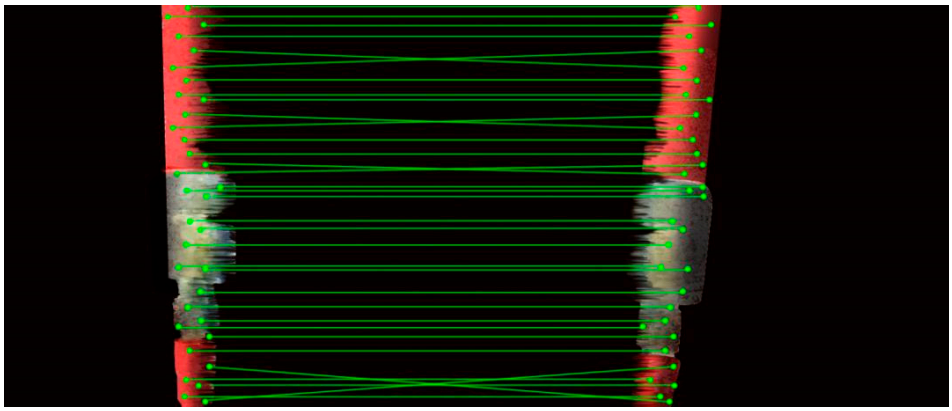

Figure 8. Feature point reverse matching.

According to Figure 8, the number of incorrectly matched point pairs decreased to a certain extent. The remaining incorrectly matched point pairs were caused by false assumptions and measurement factors. Therefore, a random sampling consistency algorithm was used. In this algorithm, denoising was performed iteratively. According to the robust matching, incorrect matching point pairs were completely eliminated. The image matching was then completed.

The experimental results of the feature point exact matching are shown in Figure 9. Thereafter, 3D point cloud stitching of the adjacent infrared cable images was performed.

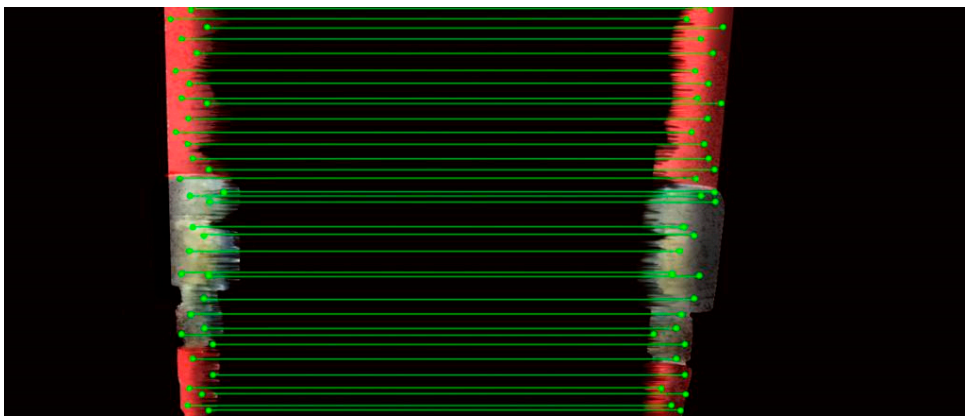

Figure 9. Feature point exact matching.

3. Infrared Stereo Vision Detection of Cable Fault Points

In this study, pure low-density polyethylene (LDPE), nano-ZnO/LDPE, and nano-methylcyclopentadienyl manganese tricarbonyl (MMT)/LDPE samples were subjected to dielectric spectroscopy. The breakdown properties of different cable insulation materials were evaluated macroscopically. Based on the combination of the thermal breakdown formation mechanism and anomalous temperature measurements in the infrared cable images, the thermal breakdown properties of different cable insulation materials were further verified. Long-distance infrared cable images were acquired in two steps. First, feature points were extracted using a multi-scale Harris operator. Second, 3D point cloud stitching was performed. The experimental results were then qualitatively analyzed.

3.1. Thermal Breakdown Property Test of Different Cable Insulation Materials

As cable working hours elapse, thermal breakdown occurs in the cable insulation material because of dielectric losses in the material. Under the effect of an external electric field, the temperature of the material increases. As a result, the insulation performance of the material becomes poor. The three main factors that cause thermal breakdown are the external voltage, working time, and material temperature. The thermal breakdown properties of different cable insulation materials can be evaluated using dielectric spectrum experiments.

The heating of the insulation materials is caused by dielectric losses. Dielectric losses include leakage currents, structural losses, polarization losses, and gas ionization losses. As the temperature increases, the thermal breakdown strength of the insulation materials decreases significantly. This occurs because the internal current loss generates heat that cannot be rejected completely and in a timely manner. Electrical treeing occurs in the insulation materials and causes thermal distortions. Finally, thermal breakdown occurs when the material temperature increases continuously. Therefore, dielectric loss detection can be used to effectively evaluate the thermal breakdown strength of insulation materials. The dielectric constant is the main parameter used to define the dielectric losses. In the dielectric frequency spectrum experiments conducted in this study, the test materials were pure LDPE, nano-ZnO/LDPE, and nano-MMT/LDPE. The test frequency of the dielectric frequency spectrum was set to 1–10^5 Hz. When the frequency of the dielectric frequency spectrum changed, the relative dielectric constant of the polymers also changed to a certain degree. The tangent of the dielectric loss angle also changed. The trilateral position exhibited a positive correlation. The relationship between the relative dielectric constant of the materials and the test frequency is shown in Figure 10.

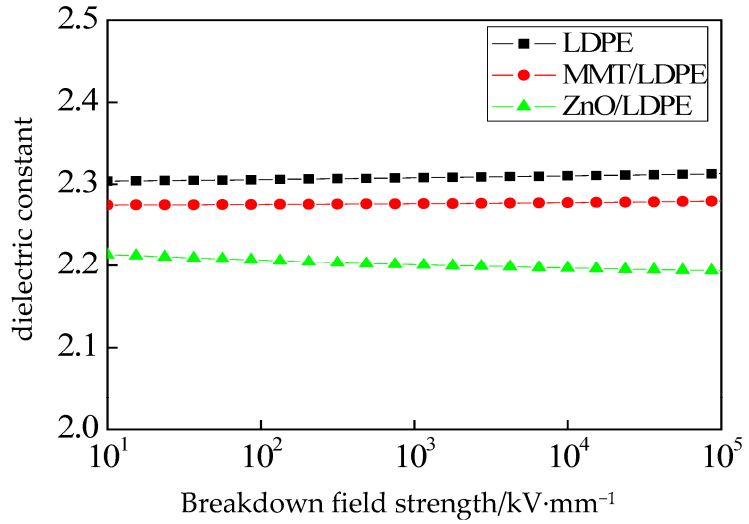

Figure 10. Frequency dependences of relative dielectric constant of various samples.

According to Figure 10, as the frequency of the dielectric frequency spectrum increased, the relative dielectric constant ε of the three test samples decreased. The trends in these

samples were consistent. According to the polarization establishment process, the properties of the three test materials were similar. The dielectric constants of nano-ZnO/LDPE and nano-MMT/LDPE are lower than those of pure LDPE. Under the applied electric field, the dielectric loss of nano-ZnO/LDPE was the lowest. This material maintained good thermal breakdown strength and insulation properties. From another perspective, the abnormal temperatures in the cable insulation layer were caused by dielectric losses. The probabilities of thermal breakdown at these points were very high. Abnormal temperatures were detected using infrared images, which can remove the hidden danger of thermal breakdown in the cable insulation layer.

3.2. Experimental Device Construction

The thermal breakdown conditions of the different high-voltage cables were tested. A stable high-voltage power supply and a series of resonant devices were used. This test environment was relatively simple and safe. Resonance phenomena occur as the frequency range, resonant reactor, and capacitor are adjusted. A high-voltage current was generated in the tested cables. Wiring schematics of the cable series resonance are shown in Figure 11.

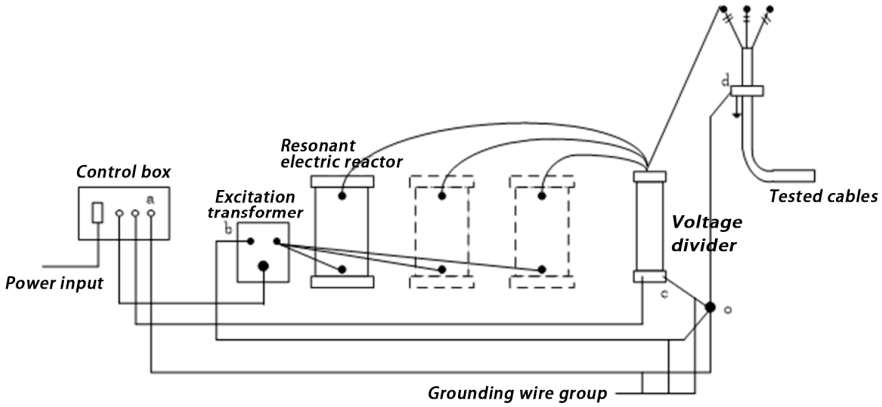

Figure 11. Schematic of cable series resonance connections.

After the series resonant device was constructed, the tested cables were energized. For the 3D stereoscopic infrared vision cable measurements, the hardware device included two infrared cameras, a double camera tripod, and a computer. The on-site setup of the system is shown in Figure 12. With the software development of MATLAB, the temperature abnormal points in collected infrared images can be identified and extracted directly according to brightness.

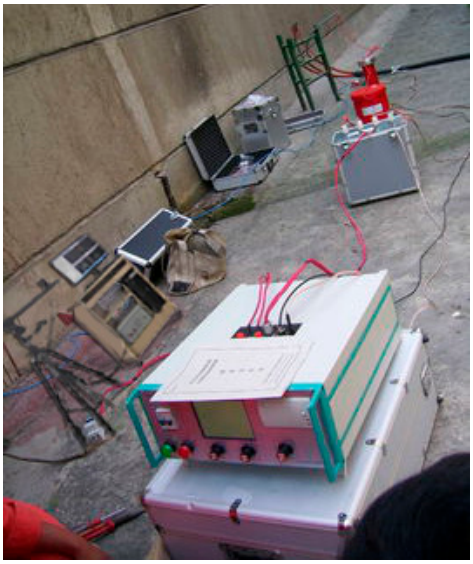

Figure 12. Experimental setup of the system used for detecting the thermal properties of the cables.

To compare the thermal breakdown conditions of the three different cable insulation layers, the cables were fixed on one fixture. The three test cables were energized simultaneously using the series resonant device. The test voltage was set to 320 kV.

3.3. Stitching Experiment and Abnormal Temperature Detection

Owing to the 6 mm infrared camera lens boundedness (the shooting range is less than 40 m), the test cables were measured in segments A and B. From three angles, information on the high-voltage cables was fully collected using an infrared camera. A comparison of the debugging effects showed that the measurement effect had the most impact when the infrared camera acquired images at a rotation angle of 120°. The 3D stereoscopic reconstruction results for the segment A and B cables at the three angles are shown in Figures 13 and 14, respectively.

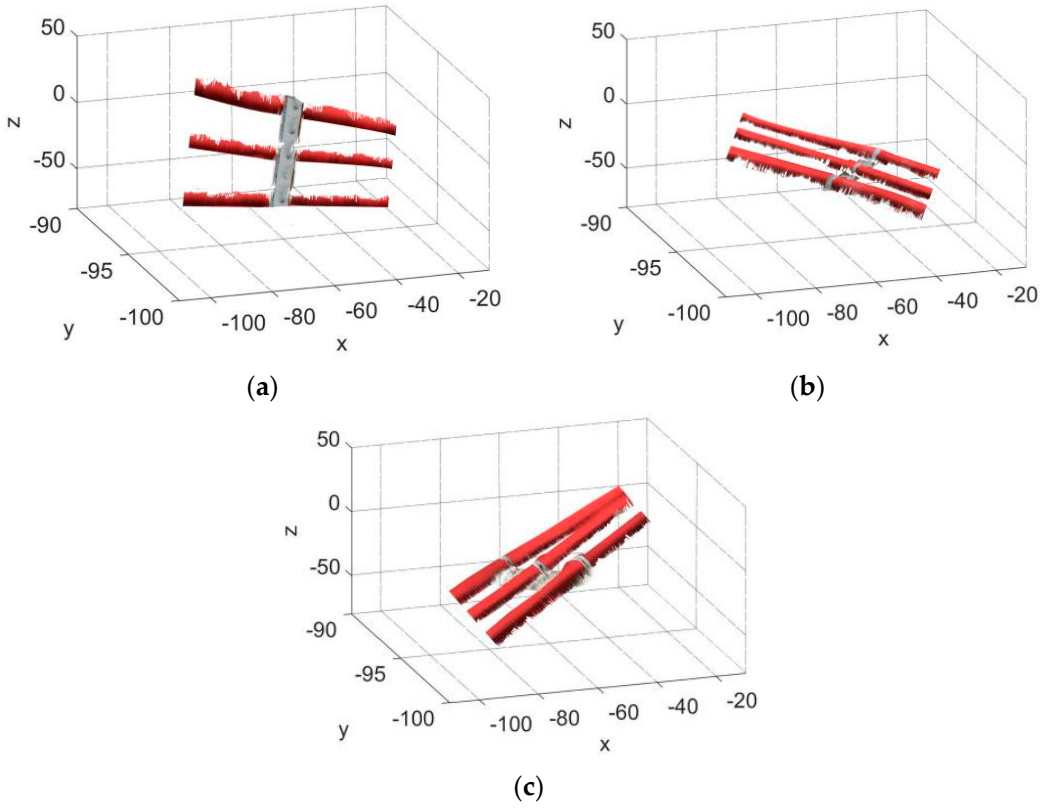

Figure 13. Three-dimensional measurements of segment A cables at three angles: (**a**) visual angle one; (**b**) visual angle two; (**c**) visual angle three.

According to the 3D reconstruction results for the infrared cable images, there were a number of abnormal temperatures in the cables that caused thermal breakdown. To accurately locate these points, an infrared stitching experiment was conducted.

High-voltage cables are large objects with identical surface shapes. It was difficult to determine the exact locations of the abnormal temperatures in the entire cable using the tested single-segment cable images. For experimental practicality, after single-segment cable image stitching, the 3D stereoscopic images of all the single-segment cables were processed with length stitching. Consequently, the abnormal temperatures in the cables were located quickly. The stitched infrared images of the segment A cables at each angle are shown in Figure 15.

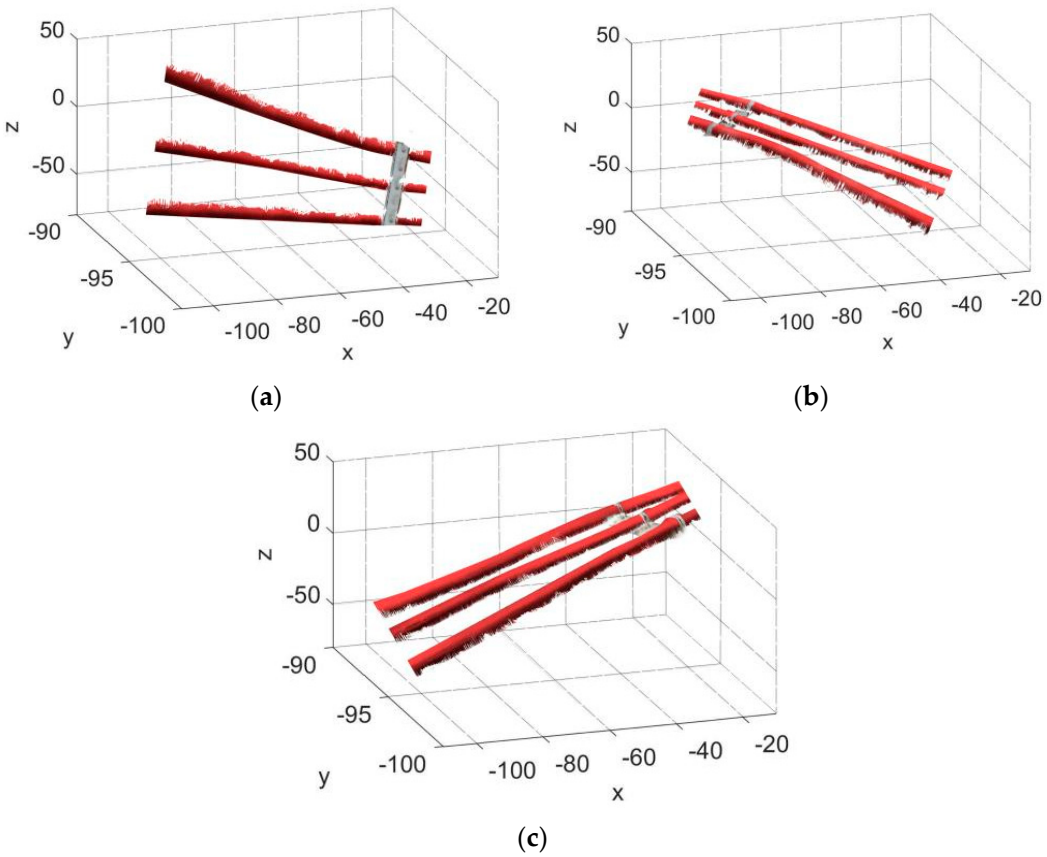

Figure 14. Three-dimensional measurements of segment B cables at three angles: (**a**) visual angle one; (**b**) visual angle two; (**c**) visual angle three.

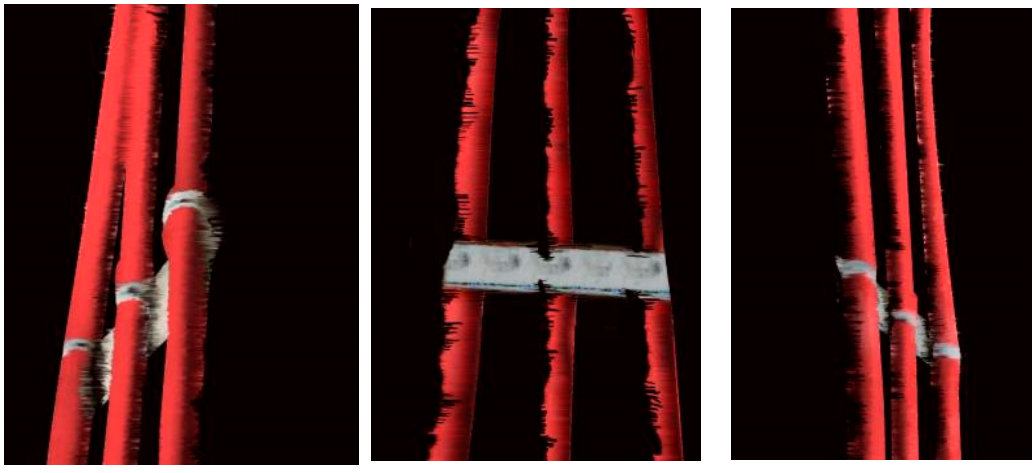

Figure 15. Stitched segment A cable images: (**a**) angle one; (**b**) angle two; (**c**) angle three.

Because the diameter of the measured object was small, the infrared stereoscopic image stitching from three angles completely captured the entire information of the segment A cables. The stitching results for the segment A cable images taken from the three angles are shown in Figure 16.

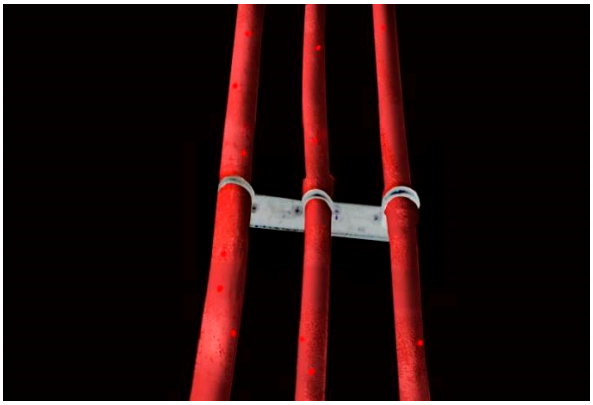

Figure 16. Stitching results for the segment A cable images.

To reflect the stitching effect, the entire cable was divided into two segments for the measurements. If the stitching effect is satisfactory, the stitching technology can be used in large-scale cable detection. The stitched infrared images of the segment B cables at each angle are shown in Figure 17.

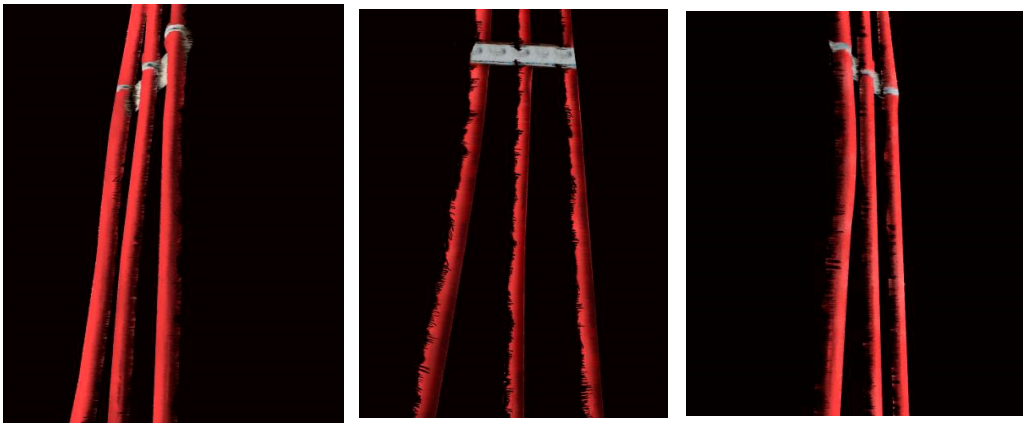

(**a**) (**b**) (**c**)

Figure 17. Stitched segment B cable images: (**a**) angle one; (**b**) angle two; (**c**) angle three.

The stitching results for the segment B cable images taken from the three angles are shown in Figure 18. The 3D infrared images of the two cable segments were subjected to length stitching. The feature point matching effect is shown in Figure 19.

Figure 18. Stitching results for the segment B cable images.

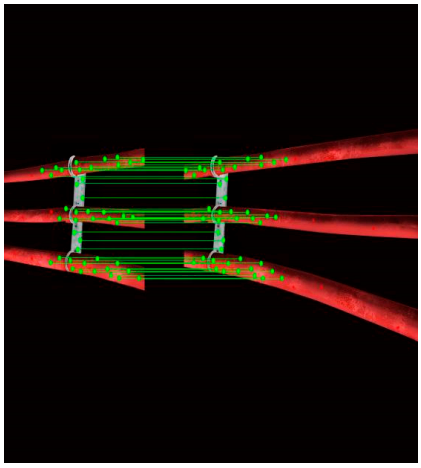

Figure 19. Feature point matching of segment A and B cable images.

According to Figure 19, the feature point matching effect of the 3D stereoscopic infrared cable images is satisfactory, as reflected by the fact that it effectively removed the noise interference. Therefore, long-distance cables can be handled using length stitching. The final experimental stitching results are shown in Figure 20.

Figure 20. Length stitching of segment A and B cable images.

According to Figure 20, the stitching effect was satisfactory. The stitching surface curve was smooth and efficiently reflected the stereoscopic characteristics of the infrared cable images. Based on these experimental results, the stitching technology can be used for large-scale cable detection.

The three tested cables were fastened to a fixture. From left to right, the cable insulation materials were pure LDPE, nano-MMT/LDPE, and nano-ZnO/LDPE. In the long-distance 3D stereoscopic infrared cable image stitching experiment, there were abnormal temperatures in each cable. This occurred because the dielectric loss of the material decreased the conductivity. In addition, heat generated over time could not be excluded. Electrical treeing occurred in the insulation materials, which generated thermal distortions. Therefore, the temperature of the materials increased continuously. The infrared images were gray processed using MATLAB software. According to the change in the gray values, the crimson areas (which represented abnormal temperatures) were extracted. This is illustrated in Figure 21. The number of abnormal temperatures and the ratio of abnormal temperature areas in the cables are shown in Table 1.

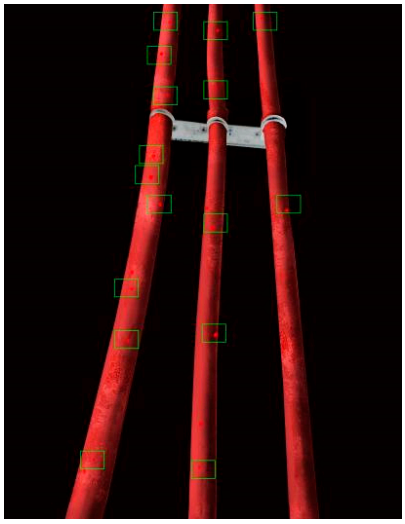

Figure 21. Results of abnormal temperature extraction in different infrared cables image.

Table 1. Comparison of anomalous temperatures measured in the cable images.

Cable Insulation Material	Anomalous Temperature Points (Number)	Ratio of Temperature Abnormal Areas in Cable Surface (%)
Pure LDPE	9	1.8
Nano-ZnO/LDPE	5	1.1
Nano-MMT/LDPE	2	0.2

According to the abnormal temperature detection results, the quantity and ratio of abnormal temperatures were the highest for the pure LDPE cables. According to the dielectric constant calculations, the thermal breakdown strength of the pure LDPE was the lowest. Therefore, during normal operations, thermal breakdown occurred easily in the LDPE cable insulation layers. However, for the nano-ZnO/LDPE composites, the quantity and ratio of abnormal temperatures were lower. The thermal breakdown strength of pure LDPE was higher. Therefore, the thermal breakdown ratio of the nano-ZnO/LDPE was lower. For the nano-MMT/LDPE composites, the number and ratio of abnormal temperatures were the lowest, and the thermal breakdown strength of this material was the highest.

4. Conclusions

In this study, to achieve online detection of cable insulation properties, cable thermal breakdown detection was carried out using infrared stereoscopic vision measurements. Three-dimensional reconstruction was performed, and infrared images were point cloud stitched. Infrared camera calibration, image correction, feature point extraction, and image stereo matching were also conducted. The conclusions of this study are as follows.

(1) A self-calibration algorithm based on subpixel feature point extraction was explored, and an experimental template for the infrared camera calibration was designed. The infrared images were corrected using a coplanar line alignment. According to the experimental results, line alignment was observed in the corrected images, and the correction was satisfactory.

(2) A multi-scale Harris operator was used to extract 3D image feature points. These feature points exhibited high precision and a uniform distribution, which met the stitching requirements. Rough matching was performed using a region-matching algorithm, which was used to search for the approximate stitching position. Accurate matching of feature points was performed using the normalized cross-correlation method. The error-matching points were eliminated using a random sampling consis-

tency algorithm. According to the qualitative observations, after image stitching, the stitching surface exhibited smooth edges and a complete structure.

(3) Pure LDPE, nano-ZnO/LDPE, and nano-MMT/LDPE were subjected to dielectric spectroscopy. From a macroscopic perspective, the thermal breakdown strength of the nano-MMT/LDPE was the highest. Electricity was supplied to the tested cables using a cable series device. Subsequently, an infrared detection experiment on the cable insulation layers was conducted. According to the test results, the number of abnormal temperatures in the nano-MMT/LDPE was the lowest.

Author Contributions: Conceptualization, Y.C. and G.Y.; methodology, G.Y.; software, Y.H.; validation, G.Y.; formal analysis, G.Y.; investigation, Y.C.; resources, Y.H.; data curation, G.Y.; writing—original draft preparation, G.Y.; writing—review and editing, G.Y.; visualization, Y.C.; supervision, Y.H.; project administration, Y.C.; funding acquisition, Y.H. All authors have read and agreed to the published version of the manuscript.

Funding: This research was aided by the key area campaign of regular universities in Guangdong province, No. 2021ZDZX1058. The Feature Innovation project of regular universities in Guangdong province, No. 2022KTSCX194. The offshore wind power joint funding project in Guangdong province, No. 2023A1515240063.

Institutional Review Board Statement: Not applicable.

Informed Consent Statement: Not applicable.

Data Availability Statement: Data is contained within the article.

Conflicts of Interest: There are no conflicts of interest.

References

1. Song, S.W.; Zhao, H.; Yao, Z.H.; Yan, Z.Y. Enhanced Electrical Properties of Polyethylene_graft-Polystyrene/LDPE Composites. *Polymers* **2020**, *12*, 124. [CrossRef] [PubMed]
2. Qiu, Y.; Zhou, S.Y.; Gu, W.; Zhang, X.P. Analysis of China's Electricity Price and Electricity Burden of Basic Industries Under the Carbon Peak Target Before 2030. *CSEE J. Power Energy Syst.* **2024**, *10*, 481–491.
3. Vijayalakshmi, S.; Deepalaxmi, R.; Rajini, V. Electromechanical characterization of titanium-dioxide-filled SiR-EPDM blends. *Polym. Polym. Compos.* **2021**, *29*, 311–322. [CrossRef]
4. Zhao, H.; Zhang, Z.L.; Yang, Y.; Xiao, J.Y. A Dynamic Monitoring Method of Temperature Distribution for Cable Joints Based on Thermal Knowledge and Conditional Generative Adversarial Network. *IEEE Trans. Instrum. Meas.* **2023**, *72*, 4507014. [CrossRef]
5. He, X.Z.; Rytoluoto, I.; Anyszka, R.; Mahtabani, A.; Saarimaki, E. Silica Surface-Modification for Tailoring the Charge Trapping Properties of PP/POE Based Dielectric Nanocomposites for HVDC Cable Application. *IEEE Access* **2020**, *8*, 87719–87734. [CrossRef]
6. Zhang, Z.Y.; Huang, Q.L.; Geng, J.H.; Liu, Q.Y.; Zhang, S.M. Defect Identification of Composite Insulator Based on Infrared Image. *Polymers* **2022**, *14*, 2620. [CrossRef] [PubMed]
7. Kim, M.G.; Jeong, S.; Kim, S.T.; Oh, K.Y. Anomaly Detection of Underground Transmission-Line through Multiscale Mask DCNN and Image Strengthening. *Mathematics* **2023**, *11*, 3143. [CrossRef]
8. Wen, F.; Jin, J. Detection of Superficial Defects in the insulation Layers of Aviation Cables by Infrared Thermographic Technique. *Coatings* **2022**, *12*, 745. [CrossRef]
9. Li, Z.M.; Yang, H.; Yang, F.; Tan, T.; Lu, X.; Tian, J. An Infrared Image based State Evaluation Method for Cable Incipient Faults. *Electr. Power Syst. Res.* **2022**, *210*, 108148. [CrossRef]
10. Mu, L.X.; Xu, X.B.; Xia, Z.N.; Yang, B.; Guo, H.R.; Zhou, W.N.; Zhou, C.K. Autonomous Analysis of Infrared Images for Condition Diagnosis of HV Cable Accessories. *Energies* **2021**, *14*, 4316. [CrossRef]
11. Kim, H.R.; Park, J.H.; Jeon, H.W.; Shin, J.S. Electromagnetic Susceptibilty design of High-Speed Image Signal Processing Unit for Small Infrared Image Homing Sensor. *J. Internet Broadcast. Commun.* **2022**, *22*, 27–33.
12. Feng, J.P.; Li, J.L.; Gao, K.; Wu, G.; Tian, J.; Zou, Y.Q. Portable Automatic DetectionSystem with Infrared Imaging for Measuring Steel Wires Corrosion Damage. *Autom. Constr.* **2023**, *156*, 105150. [CrossRef]
13. Liao, Y.; Jiang, X.L.; Zhang, Z.J.; Zheng, H.L.; Li, T. The influence of Wind Speed on the Thermal Imaging Clarity Based Inspection for Transmission Line Conductors. *IEEE Trans. Power Deliv.* **2023**, *38*, 2101–2109. [CrossRef]
14. Zhang, J.W.; Zhang, Z.G.; Liu, B. Non-destructive Testing of Steel Wire Ropes Incorporating Magnetic Memory Information. *Insight* **2023**, *65*, 87–94. [CrossRef]
15. Zhang, J.W.; Chen, Q.K.; Ye, Q. Nondestructive Testing of Steel Wire Rope Based on Gagnetic Signal and Infrared Information. *Russ. J. Nondestruct. Test.* **2023**, *59*, 991–1004. [CrossRef]

16. Li, Y.; Zheng, J.; Wang, F.N.; Hu, C.W.; Yang, F.; Ma, X.G. Movement and Deformation Characteristics of Overlying Rock Mass in Deep Coal Seam. *J. Mt. Sci.* **2023**, *20*, 1725–1741. [CrossRef]
17. Fernandez, I.; Torres, G. Thermographic assessment of skin response to strength training in young participants. *J. Therm. Anal. Calorim.* **2023**, *148*, 3407–3415. [CrossRef]
18. Li, R.Z.J.; Wang, Z.G.; Sun, H.Q. Automatic Identification of Earth Rock Embankment Piping Hazards in Small and Medium Rivers Based on UAV Thermal Infrared and Visible Images. *Remote Sens.* **2023**, *15*, 4492. [CrossRef]
19. Zhou, W.; Ji, C.; Fang, M. Effective Dual-Feature Fusion Network for Transmission Line Detection. *IEEE Sens. J.* **2024**, *24*, 101–109. [CrossRef]
20. Deng, Y.; Zhu, K.H.; Zhao, G.J.; Zhu, J.Y. Efficient Partial Discharge Signal Denoising Method via Adaptive Variational Modal Decomposition for Infrared Detectors. *Infrared Phys. Technol.* **2022**, *125*, 104230. [CrossRef]
21. Zhang, Z.G.; Zhang, J.W. Quantitative Nondestructive Testing of Broken Wires for Wire Rope Based on Multi-Image Fusion. *Russ. J. Nondestruct. Test.* **2022**, *58*, 643–656. [CrossRef]
22. Liu, T.; Li, G.L.; Gao, Y. Fault Diagnosis Method of Substation Equipment based on You Only Look Once Algorithm and Infrared Imaging. *Energy Rep.* **2022**, *8*, 171–180. [CrossRef]
23. Gao, Y.F.; Yang, J.; Zhang, K. A New Method of Conductor Galloping Monitoring Using the Target Detection of Infrared Source. *Electronics* **2022**, *11*, 1207. [CrossRef]
24. Yang, L.; Kong, S.Y.; Huang, H.Y.; Li, H.; Fang, L.; Povey, D.; Zhai, G.; Mei, T.; Wang, R. TAR-Net A Triple Attention Residual Network for Power Line Extraction from Infrared Aerial Images. *Artif. Intell. CICAI PTI* **2022**, *13604*, 647–657.
25. Lyra, S.; Rixen, J.; Heimann, K.; Karthik, S.; Joseph, J.; Jayaraman, K.; Orlikowsky, T. Camera Fusion for Real-time Temperature Monitoring of Neonates Using Deep Learning. *Med. Biol. Eng. Comput.* **2022**, *60*, 1787–1800. [CrossRef] [PubMed]
26. Wu, Z.Y.; Qin, S.; Zhang, P.Y.; Pan, Z.X.; Hu, X.D.; Shi, L. Damage Evolution in Braided Composite Tubes Under Axial Compression Studied by Combining Infrared Thermography and X-ray Computed Tomography. *Compos. Struct.* **2023**, *307*, 116634. [CrossRef]
27. Carrasco, R.; Lapayese, F.; Dela, A.; Medrano, M.; Mota, F.; Soleto, A.; Pereira, A.; Pastor, C.; Rodriguez, C.; Rincon, E. Test on the prototype of the Optical Hinge for the Wide Angle Viewing System to ITER Gamma Radiation Conditions. *Fusion Eng. Des.* **2023**, *193*, 113680. [CrossRef]
28. Nooralishahi, P.; Rezayiye, R.K.; Lopez, F.; Maldague, X. PHM-IRNET: Self-training Thermal Segmentation Approach for Thermographic Inspection of Industrical Components. *NDT Int.* **2023**, *138*, 102884. [CrossRef]
29. Lin, Z.Y.; Xie, J.L.; Zhang, Q.F.; Xu, M.M.; Zeng, Q.B. Stray Light Suppression for Thomson Scattering Diagnostics on Linear Magnetized Plasma Device. *J. Instrum.* **2023**, *18*, C11002. [CrossRef]
30. Zhu, S.W.; Wu, S.X.; Fu, Y.; Guo, S.X. Prediction of particle-reinforced composite material properties based on an improved Halpin-Tsai model. *AIP Adv.* **2024**, *14*, 045339. [CrossRef]
31. Yin, Y.H.; Yu, Q.F.; Hu, B.; Zhang, Y.Q.; Chen, W.J.; Liu, X.L.; Ding, X.H. A Vision Monitoring System for Multipoint Deflection of Large-span Bridge based on Camera Networking. *Comput.-Aided Civ. Infrastruct. Eng.* **2023**, *38*, 1879–1891. [CrossRef]
32. Mehmood, I.; Li, H.; Umer, W.; Ma, J.; Shakeel, M.S.; Anwer, S.; Antwi, M.F. Non-invasive detection of mental fatigue in construction equipment operators through geometric measurements of facial features. *J. Saf. Res.* **2024**, *89*, 234–250. [CrossRef] [PubMed]
33. Zhang, W.N.; Zhao, Y.Q. An improved SIFT algorithm for registration between SAR and optical images. *Sci. Rep.* **2023**, *13*, 33532. [CrossRef] [PubMed]
34. Qi, Q.Y.; Huang, W.S.; Zhang, D.H.; Han, L.G. Robust Elastic Full-Waveform Inversion Based on Normalized Cross-Correlation Source Wavelst Inversion. *Appl. Sci.* **2023**, *13*, 13014. [CrossRef]